Direct Numerical Simulation of Fully-Saturated Flow in Natural Porous Media at the Pore-Scale: A Comparison of Three Computational Systems

M. Siena[1], J. D. Hyman[2,4], M. Riva[1,3], A. Guadagnini[1,3], C. L. Winter[3,4], P. K. Smolarkiewicz[5], P. Gouze[6], S. Sadhukhan[6], F. Inzoli[7], G. Guédon[7], E. Colombo[7]

[1]Dipartimento di Ingegneria Civile e Ambientale, Politecnico di Milano, Milano, 20133, Italy.

[2]Computational Earth Science, Earth and Environmental Sciences and the Center for Non-Linear Studies, Los Alamos Nat'l Lab., Los Alamos, NM 87545, USA

[3]Department of Hydrology and Water Resources, University of Arizona, Tucson, AZ 85721, USA

[4]Program in Applied Mathematics, University of Arizona, Tucson, AZ 85721, USA

[5]European Centre for Medium-Range Weather Forecasts, Reading, UK

[6]Géosciences, Université Montpellier - CNRS, Montpellier, 34095, France

[7]Dipartimento di Energia, Politecnico di Milano, Milano, 20133, Italy

Corresponding author: Martina Siena

Email: martina.siena@polimi.it,

Ph: +39 02 2399 6293

Fax: +39 02 2399 6298

1

Abstract

Direct numerical simulations of flow through two millimeter-scale rock samples of limestone and sandstone are performed using three diverse fluid dynamics simulators. The resulting steady-state velocity fields are compared in terms of the associated empirical probability density functions (PDFs) and key statistics of the velocity fields. The pore-space geometry of each sample is imaged at 5.06 μm voxel-size resolution using X-ray micro-tomography. The samples offer contrasting characteristics in terms of total connected porosity (about 0.31 for the limestone and 0.07 for the sandstone) and are typical of several applications in hydrogeology and petroleum engineering. The three-dimensional fluid velocity fields within the explicit pore spaces are simulated using ANSYS® FLUENT® [ANSYS, Inc.: ANSYS® FLUENT® User's guide, Rel. 12.1, (2009)], EULAG [Prusa, J.M., Smolarkiewicz, P.K., Wyszogrodzki, A.A.: Comput. Fluids 37, 1193 (2008)], and SSTOKES [Sarkar, S., Toksöz, M.N., Burns, D.R.: Annual Consortium Meeting MIT Earth Resources Laboratory (2002)]. These computational approaches are highly disperse in terms of algorithmic complexity, differ in terms of their governing equations, the adopted numerical methodologies, the enforcement of internal no-slip boundary conditions at the fluid-solid interface, and the computational mesh structure. As metrics of comparison to probe in a statistical sense the internal similarities/differences across sample populations of velocities obtained through the computational systems, we consider (*i*) integral quantities, such as the Darcy flux, and (*ii*) main statistical moments of local velocity distributions including local correlations between velocity fields. Comparison of simulation results indicates that mutually consistent estimates of the state of flow are obtained in the analyzed samples of natural pore spaces, despite the considerable differences associated with the three computational approaches. We note that in the higher porosity limestone sample, the structures of the velocity fields obtained using ANSYS FLUENT and EULAG are more alike than either compared against the results obtained using SSTOKES. In the low porosity sample, the structures of the velocity fields obtained by EULAG and SSTOKES are more similar than either is to the fields obtained using ANSYS FLUENT. With respect to macroscopic quantities, ANSYS FLUENT and SSTOKES

provide similar results in terms of the average vertical velocity for both of the complex micro-scale geometries considered, while EULAG tends to render the largest velocity values. The influence of the pore space structure on fluid velocity field characteristics is also discussed.

Keywords Pore-scale flow simulation, Porous media, Eulerian grid-based methods, Computational models comparison, Immersed boundary method.

1 Introduction

Recent developments in pore-scale modeling and imaging techniques are playing a key role in our understanding of the feedback between small-scale physics and macro-scale modeling of flow and transport processes in natural and/or reconstructed porous media [18, 28]. In particular, high-resolution mapping and visualization of the structure of geologic materials allow detailed pore-scale modeling of flow in topologically complex pore spaces. Direct numerical simulation of flow through intricate microscopic structures yields insights into the effects of pore space characteristics on both microscopic and macroscopic flow properties. Modeling these phenomena has applications that range from groundwater flow and transport [29], to geophysics, including, e.g., petroleum extraction [28] and carbon sequestration [4], to filter design [15]. The spatially variable resistance to flow offered by the solid phase of a porous medium induces non-uniform fluid velocity fields where the observed dynamics range from stagnation to chaotic separation of fluid particle trajectories [19]. The effects of these flows taking place at the micro-scale can be embedded into continuum scale models, which can then be used to support field-scaled decision-making in oil, gas, and groundwater reservoir management.

As opposed to a pore-network modeling approach [4, 5, 34, 47] or a particle-based Lagrangian methodology, e.g., lattice-Boltzmann [6, 8, 9, 16, 23, 26, 30] and smoothed particle hydrodynamics [44, 45], in the Eulerian methodology for simulating flow in microscopic pore structures a particular numerical scheme, such as finite difference [26], finite element [10] or finite volume [11, 49], is selected and the governing equations of flow are discretized accordingly. This discrete approximation

is then numerically integrated on a computational mesh representing the pore space in a direct numerical simulation of flow. Comparisons of direct simulations of single-phase flow with particle-based methods [11,26] revealed minimal and essentially negligible differences between the results obtained with the methodologies tested, but a clear advantage of the Eulerian methods was observed with regard to the required computation time. Lagrangian methods are slow to converge to a steady-state solution (for cases when the system evolves to attain steady-state) even when the codes are highly parallelized [9, 16].

Here, we compare three methodologies for the direct numerical simulation of gravity-driven, fully-saturated, single-phase flow at the pore microstructure scale in two millimeter-scale natural rock samples. All three models are comparable in terms of resolution, but they are fundamentally dissimilar in terms of numerical methodologies and algorithmic complexity. We consider (*a*) the ANSYS® FLUENT® software [2], which integrates the Navier-Stokes equations using a finite volume method on a hexagonal mesh; (*b*) the EULAG system [33], which uses conservative finite differences coupled with the volume-penalizing immersed boundary (IB) methodology to resolve the Navier-Stokes equations on a uniform Cartesian grid; and (*c*) the SSTOKES software, which uses standard second order finite differencing and the ghost-cell IB method proposed by [35] to resolve the Stokes equations on meshes composed of cubic voxels. The natural porous media samples we consider consist of a quasi-pure silica sandstone and an oolithic limestone, which are characterized by distinctly different pore-scale structures. These types of geo-materials are found in several hydrogeology and petroleum engineering applications, and are viewed as typical media for the oil and gas industry. A detailed reconstruction of the pore-space geometry of these systems was performed using X-ray micro-tomography [14], which provides information about the internal structure of natural samples in a non-destructive way [48].

Quantification of similarities/differences is performed according to (*i*) integral quantities, such as the Darcy flux, as well as (*ii*) the structure of the velocity distributions, characterized through their empirical probability density function (PDF) and the associated key statistical moments, including

local correlations between velocity fields. These measurements are employed to probe in a statistical sense the internal similarities/differences across sample populations of velocities obtained for the two porous media analyzed using the three different computational systems. While the adopted methodologies are notably contrasting in terms of numerical schemes, our results show that they all produce results that are reasonably close to one another. In the case of the limestone sample, the structures of the velocity fields obtained using ANSYS FLUENT and EULAG are more alike than either with that obtained using SSTOKES. In the case of the sandstone sample, the structures of the velocity fields obtained by EULAG and SSTOKES are more like one another than either to the solution obtained using ANSYS FLUENT. So far as macroscopic quantities are concerned, ANSYS FLUENT and SSTOKES provide similar results in terms of the average vertical velocity for both of the complex micro-scale geometries considered, while EULAG tends to render larger velocity values with greater variability. The documented correspondence among the results supports the reliability of computational approaches to detailed pore-scale simulations.

The remainder of the paper is divided into three main sections. Section 2 describes the two natural rock samples and the three modeling approaches in terms of geometrical description, mathematical formulation, and numerical techniques. Section 3 is devoted to the comparison of the results from the three different methodologies in terms of local and integral quantities. Concluding remarks are presented in Section 4.

2 Methods

2.1 *Description of rock samples*

We study flow through samples of two different (natural) rocks: (*a*) an oolitic limestone from the Mondeville formation of the middle Jurassic age, and (*b*) a Fontainebleau sandstone, both from the Paris Basin (France). The overall dimensions of the analyzed blocks are $0.65\times0.65\times1.3$ mm^3, and we refer to them as the limestone sample and the sandstone sample. The limestone is composed of millimeter-scale recrystallized ooliths, partially cemented with micritic calcite [13]. The limestone sample was subject to carbonate dissolution performed under laboratory conditions that increased the

105 total connected porosity of the sample from about $\phi_L \approx 6.8\%$ to $\phi_L = 31.41\%$. The sandstone is a
106 quasi-pure silica sandstone that is often used as a standard analog for sandstone reservoirs. Porosities
107 of samples of these sandstones usually range from 5% to 30%, and grain sizes are relatively
108 homogeneous, typically around 250 μm [7]. The sandstone sample is characterized by a total
109 connected porosity $\phi_S = 7.05\%$. The porosity values provided here represent the connected pore
110 network, i.e., the void space that connects the flow inlet and outlet boundaries.

111 The three-dimensional structure of each sample is reconstructed via synchrotron X-ray micro-
112 tomography, with a voxel size of $\Delta z = 5.06$ μm [14]. Both samples were imaged using the ID19 beam
113 at the European Synchrotron Radiation Facility (Grenoble, France). Figure 1a illustrates the structure
114 of the pore space of the limestone sample by means of a set of horizontal cross sections; Fig. 1b shows
115 the vertical profile of surface porosity (each value is associated with a volume of size 0.65 mm $\times$ 0.65
116 mm $\times \Delta z$) and Fig. 1c depicts the sample probability density functions of pore sizes, *S*, normalized by
117 the grid step, evaluated along the three Cartesian axes, *x*, *y* and *z* and computed on the whole domain
118 according to the methodology employed in [37]. Figure 2 depicts graphically the corresponding set
119 of information for the sandstone rock.

120 Surface porosities computed along horizontal planes range between 13% and 50% for the
121 limestone and between 1.4% and 23% for the sandstone. Each sample exhibits an abrupt change in
122 porosity starting a little further than midway down the sample column and ending well before the
123 bottom, the limestone showing an anomalous region of low porosity and the sandstone showing an
124 anomalously high porosity region. The empirical Probability Density Functions (PDFs) of pore sizes
125 (Figs. 1c and 2c) reveal that each system is relatively isotropic. When plotted on a semi-logarithmic
126 scale, the PDF tails display a clear exponential decay for an intermediate range of pore size values,
127 analogously to what observed by [37] for synthetically generated pore structures. The range covered
128 by the pore size values in the limestone (i.e., the medium with largest porosity) is wider than in the
129 sandstone in all directions.

130 ### 2.2 *Mathematical formulation of the flow problem*

131 The governing equations for a single-phase, incompressible Newtonian fluid, i.e., water, fully-
132 saturating the pore space, are the transient Navier-Stokes equations,

133 $$\nabla \cdot \mathbf{v} = 0 \tag{1}$$

134 $$\frac{\partial \mathbf{v}}{\partial t} + \mathbf{v} \cdot \nabla \mathbf{v} = -\frac{1}{\rho} \nabla p' + \mathbf{g} + \nu \Delta \mathbf{v} \tag{2}$$

135 Here, Eqs. (1) and (2) respectively represent mass and momentum conservation; $\mathbf{v}$ is the Eulerian
136 fluid velocity vector, ν is fluid kinematic viscosity, ρ is fluid density, $p' = (p - p_0)$ is relative
137 pressure and $\mathbf{g} = (0, 0, -g)$ is gravity force (p, g, and p_0 respectively being pressure, gravity and a
138 constant reference pressure). Fluid density and kinematic viscosity are set respectively as $\rho = 1025$
139 kg m^{-3} and $\nu = 1 \times 10^{-6}$ m^2 s^{-1} for all simulations. No-slip boundary conditions, i.e., $\mathbf{v} = 0$, are enforced
140 along pore walls boundaries.

141 The Reynolds number associated with flow through natural fractured and porous media is
142 usually small enough to consider creeping-flow regime as a valid assumption [4, 11]. Under this
143 assumption, the nonlinear term in Eq. (2) can be disregarded, and the governing equations are the
144 incompressible Stokes equations, i.e.,

145 $$\frac{\partial \mathbf{v}}{\partial t} = -\frac{1}{\rho} \nabla p' + \mathbf{g} + \nu \Delta \mathbf{v} \tag{3}$$

146 together with Eq. (1) in the void space of the samples.

147 ### 2.3 *Problem setting*

148 Comparisons among the ANSYS FLUENT, EULAG and SSTOKES computational models are
149 performed at steady-state flow conditions for both rock samples considered. We define steady-state
150 conditions to be reached when the following criteria are met. First, the relative difference between
151 the average velocity magnitude observed at two consecutive time steps, symbolized as t and (t + 1),
152 is such that

153 $$\left| \frac{\langle |\mathbf{v}| \rangle_{t+1} - \langle |\mathbf{v}| \rangle_t}{\langle |\mathbf{v}| \rangle_t} \right| < 10^{-6} \tag{4}$$

$\langle \cdot \rangle$ being sample average evaluated over all pore voxels. Second, the difference between the vertical (i.e., along direction z) component of velocity, w, observed at two consecutive time steps at corresponding nodal locations is such that

$$\frac{\langle | w(x,y,z,t+1) - w(x,y,z,t) | \rangle}{\langle | w(x,y,z,t) | \rangle} < 10^{-6} \tag{5}$$

ANSYS FLUENT and EULAG solve Eqs. (1) and (2), while SSTOKES solves Eqs. (1) and (3). All flow simulations are performed in the discretized domains of size 128 × 128 × 256 voxels depicted in Figs. 1a and 2a. Impermeable boundary conditions are set on the lateral sides of the samples for all of the approaches. In each case flow is gravity driven (i.e., induced by **g**) and takes place predominantly in the vertical direction, z. Periodic boundary conditions are employed in EULAG, $\mathbf{v}(x, y, 0) = \mathbf{v}(x, y, L)$, along the vertical direction, together with the corresponding periodic boundary conditions for the gradient of relative pressure in Eq. (1). Benefits of considering periodic boundaries include the ability to handle blocked flows in incompressible fluid settings and to ensure compatibility of initial conditions with the governing equations. It has to be noted that ensuring flow periodicity requires the (physical) domain to be periodic. With synthetically generated virtual media, system periodicity can be achieved during the generation process [20]. Periodicity for a real rock sample is achieved by mirroring the (generally non-periodic) sample image along the vertical direction. The resulting medium is then symmetric with respect to the middle horizontal plane. The same geometric model and periodic conditions are adopted for consistency within the ANSYS FLUENT and the SSTOKES software environments. As a result of this vertical mirroring, the size of each simulated system is 128 × 128 × 512 voxels. Only the results associated with the original sample with size 128 × 128 × 256 voxels are analyzed and presented in Section 3.

2.4 *Numerical Methods*

Major challenges for the direct simulation of flow in explicit pore structures include (*a*) the representation of the complicated geometry of the porous microstructure and (*b*) the enforcement of

no-slip boundary conditions along pore walls. Accurate representation of a pore space at the scale and resolution of interest associated with a binary digital image of pore spaces can be achieved using smooth, unstructured meshes and refined octree grids that conform to the geometry of the pore space [21, 49]. These variable resolution meshes can be refined along pore walls to resolve boundary layer effects in the flow field that occur at length scales smaller than the resolution of the imaged pore spaces. Generating conformal meshes to represent the intricate geometries that make up real porous microstructures is demanding, both in terms of computer memory and computational time. A first order accurate stair-step representation of the void space, where the pore space is discretized by structured hexahedral cells or cubic voxels, offers a meshing approach that partially overcomes these demands. Although the accuracy of the representation of the solid boundary is somewhat compromised, stair-stepping yields meshes that are efficient and low cost but accurate within bounds of computational error for simulations of flow through pore microstructures [18]. Gerbaux et al. [11] compared the performance of tetrahedral and hexagonal meshes, and concluded that the latter required less computational resources, with minimal discrepancies between the flow results. Analogous results stem from pore-scale flow simulations of Peszynska and Trykozko [32], who tested unstructured hexahedral and body-fitted mesh performances within the ANSYS FLUENT software environment.

Once the mesh has been selected, no-slip boundary conditions can be directly enforced by spatially varying the difference stencil to conform with the pore space geometry. The efficient implementation of this approach still remains a critical challenge. A promising alternative is given by the immersed boundary method (IB) [27]. According to the latter, no-slip boundary conditions are enforced at the fluid-solid interface by inserting a fictitious forcing term into the governing equations of flow to mimic the resistance offered by the solid wall boundaries. The advantage of this approach is that a uniform Cartesian grid can be employed to simulate flow in complex pore spaces and the difference stencil is uniform throughout the computational domain. This uniformity makes the method well suited for existing and future HPC architectures, such as GPUs and MIC. The IB has

been successfully applied to two [24, 25] and three-dimensional [17, 18, 19, 36, 37, 43] simulations of flow in microscopic pore structures.

Immersed boundary methods are naturally divided into continuous and discrete (or direct) forcing approaches, depending on the way the fictitious forcing term is implemented. In the continuous approach, the forcing term is included in the original continuous form of the governing equations, while in the discrete approach the fictitious boundary force is introduced after the equations have been discretized. Examples of the continuous forcing class include volume penalizing [1] and feedback forcing methods [12] that set the additional forcing term to be proportional to the flow velocity. An example of the discrete-forcing class of IB approaches is the ghost cell method [31, 46] where the computational (discretized) domain is partitioned into physical and ghost-cell sub-domains. The physical sub-domain contains only computational cells associated with the fluid, whereas computational cells that reside within the solid domain and have at least one neighboring cell in the fluid phase form the ghost-cell sub-domain. Velocity values are computed for each ghost cell through interpolation so that the desired boundary conditions at the fluid-solid interface are enforced on the basis of a "projection node" located within the fluid region.

2.5 *Computational Systems*

ANSYS FLUENT. The first computational system employed in this study is embedded in the ANSYS FLUENT software and uses a finite volume method to numerically integrate Eqs. (1) and (2) on a first-order hexagonal grid representation of the fluid domain. FLUENT is a commercial code maintained by ANSYS, Inc, (www.ansys.com). A segregated transient formulation using the non-iterative Pressure Implicit Splitting of Operators (PISO) algorithm [2, 22] for pressure-velocity coupling is employed. The advection term in Eq. (2) is discretized using a second order upwind scheme developed for unstructured meshes and limiting the gradient of the advected quantity to avoid occurrence of new maxima or minima [3]. Pressure is discretized using a body force weighted scheme and linear second order accurate interpolations are used for the discretization of the viscous term [2]. All variables are collocated on the hexahedral mesh. The faces of the hexahedral elements lying at

the fluid-solid interface define the boundary position and no-slip conditions are set directly at the face center using the adopted finite volume method. The time step employed in the simulations performed with ANSYS FLUENT is $\Delta t = 2.5\times10^{-6}$ s. For this study, the code was run in parallel on 12 CPUs, on a Dell™ PowerEdge™ R410 machine, with 2x Intel® Xeon® X5670 (6 cores @ 2.93 GHz and 32 GB of Ram).

EULAG. The second system we use in this study is the modification of the EULAG system provided by Smolarkiewicz and Winter [43]. EULAG is open source and can be obtained by contacting the developers at http://www2.mmm.ucar.edu/eulag/. In this framework, no-slip boundary conditions are enforced using a continuous forcing IB method. Formally, a modification of the momentum equation (2) allows for the implicit enforcement of no-slip conditions along the fluid-solid interface,

$$\frac{\partial \mathbf{v}}{\partial t} + \mathbf{v}\cdot\nabla\mathbf{v} = -\nabla\pi' + \mathbf{g}\frac{\rho'}{\rho} + \nu\Delta\mathbf{v} - \alpha\mathbf{v} \tag{6}$$

As in Eq. (2), here primes refer to perturbations with respect to static ambient atmospheric conditions characterized by a constant density, ρ_0, and pressure, p_0, i.e., $\pi' = (p - p_0)/\rho$ and $\rho' = \rho - \rho_0$, where $\rho = const >> \rho_0$ denotes the density of water. The fictitious repelling body force, $\alpha\mathbf{v}$, is inserted in the right side of the momentum equation (2) to circumvent the difficulty of generating a conforming mesh representation of the void space. In Eq. (6), $\alpha(\mathbf{x})$ vanishes when vector location $\mathbf{x}$ is in the pore volume and is large otherwise. Intuitively, setting $\alpha(\mathbf{x}) = 0$ within the pore volume admits Navier-Stokes flows away from the solid boundaries and Eq. (6) reduces to Eq. (2); on the other hand, requiring $\alpha(\mathbf{x}) \to \infty$ within the solid prevents flow therein [41, 43]. The governing system of Eqs. (1) and (6) is cast in the conservation form and integrated numerically at every computational node in the uniform Cartesian grid using a second-order-accurate, semi-implicit, non-oscillatory forward-in-time (NFT) approach. Theoretical bases, implementation and applications of the approach are broadly documented [38, 39, 40, 42]. The NFT approach is a flux-form finite difference method, an equivalent of finite-volume approach on a Cartesian grid. The resolution is globally semi-implicit:

convective and diffusive terms are solved explicitly, whereas all the forcing terms in Eq. (6) are dealt with implicitly using a preconditioned Krylov method to solve the resulting elliptic equation. Details of the discretized set of equations and of the numerical integration procedure are found in [43]. The EULAG code is run in parallel using 8 CPUs on the Dell™ PowerEdge™ R410 machine with 2x Intel® Xeon® X5670 (6 cores @ 2.93 GHz and 32 GB of Ram) for the limestone sample and using 16 CPUs on the Dell™ PowerEdge™ R620 machine with 2x Intel® Xeon® E5-2680 (8 cores @ 2.70 GHz and 64 GB of Ram) for the sandstone. For our simulations, we follow Smolarkiewicz et al. [43] and set $\alpha^{-1} = \Delta t / 2 = 2 \times 10^{-8}$ s. This value is considerably smaller than the time scales associated with the effects of viscous and gravity forces evaluated at the grid scale, that are respectively $(\Delta z)^2 / \nu = 2.5 \times 10^{-5}$s and $(2\Delta z / g)^{1/2} = 1 \times 10^{-3}$ s.

SSTOKES. The third system we use is the SSTOKES code [35], which can be made available upon request. SSTOKES enforces internal boundary conditions using a discrete IB method, and the space and time derivatives of Eqs. (1) and (3) are discretized using second order centered-difference and forward-difference schemes respectively and solved implicitly. SSTOKES uses a staggered approach where pressure is defined at the cell center, and velocity components are considered along the cell faces. In this framework, velocities tangential to the solid boundary are not defined at the boundary itself. The ghost-cell IB method is used to enforce the no-slip boundary conditions along internal solid boundaries. At each time step, flow variables in the ghost cells outside of the void space are determined using linear interpolation with the neighboring image points inside of the void space to enforce no-slip conditions exactly along the void-solid interface. The computational mesh is a first order cubic stair-step approximation of the void space embedded within the solid phase. The computational parameters considered for the SSTOKES system are those controlling the convergence to a steady-state solution. The time step employed in the simulations performed with SSTOKES is $\Delta t = 2 \times 10^{-8}$ s. The SSTOKES code is not parallelized. In this study, it was run on one core of the HP Z800 workstation equipped with 2x Intel® Xeon® E5-2680 (8 cores @ 2.7 GHz and 64 GB Ram).

2.6 *Metrics for system comparison*

The analysis of the simulation results compares the capabilities of the three considered methodologies to simulate pore-scale flow fields in natural porous media at the millimeter scale. The local Eulerian vertical velocity component, *w*, is a key quantity of interest in the comparison due to its relevance in transport processes occurring at the scale of porous microstructure. The comparison of the steady-state flow fields is performed in terms of the structure of the velocity and pressure fields, the distribution of the vertical velocities, as well as integral quantities, namely the Darcy flux, $q(z)$ computed at steady-state, i.e.,

$$q(z) = \frac{1}{N} \sum_{i=1}^{N_P(z)} w_i \tag{7}$$

In Eq. (7), $N_P(z)$ is the number of nodes in the pore space of the horizontal plane at elevation *z*; *N* = 16384 is the total number of nodes at a given horizontal cross section; w_i is the vertical component of the Eulerian velocity calculated at node *i*. Since nowadays we still do not have at our disposal high quality laboratory flow experimental data which can be employed for a point-by-point comparison against computed values in real rock samples of the size we consider, the structures of the resulting velocity fields are also compared in terms of their empirical probability density functions (PDFs) and associated main statistics. These include the coefficient of variation related to the calculated local velocities as well as the point wise cross-correlation coefficient between vertical velocity fields at every horizontal cross-section of the system, defined as

$$R_{ij} = \frac{\left\langle \left(w_i - \langle w_i \rangle \right) \left(w_j - \langle w_j \rangle \right) \right\rangle}{\sigma_{w_i} \sigma_{w_j}} \tag{8}$$

where *i*, *j* = *E*, *S*, or *F* (*E*, *S*, or *F* respectively denoting EULAG, STOKES, or FLUENT), and $\langle w_i \rangle$ and σ_{w_i} respectively are average and standard deviation of nodal values of w_i computed across a given cross-section located at vertical elevation *z*.

When considered jointly with integral quantities, these metrics provide additional layers of information regarding the structure of the velocity fields and allow investigating in a statistical sense the similarities/differences between the distributions of velocity. The standard deviation provides information about the variability of the spatial distribution of the values of a given quantity, and the coefficient of variation is an indicator of the intrinsic variability resulting from each computational system after accounting for the multiplicative effect of the mean. The cross-correlation coefficient is a measure of the linear dependence between two variables and quantifies (in a statistical sense) the degree of similarity of the flow solutions obtained by two computational suites. A qualitative description and comparison of the contour plots of velocities of the cross sections is also provided. Flow statistics such as mean vertical velocity, standard deviation, and cross-correlation are calculated over the total number of nodes in the pore space, i.e., $N_P(z)$ within a cross-section, or $N_{P,TOT}$ for the entire volume.

3 Results

3.1 *Mondeville limestone sample*

The three computational systems produce fluid velocities that are the same order of magnitude, i.e., $O(10^{-4}\ \mathrm{m\,s^{-1}})$. The Reynolds number Re = *UL*/ν, *L* and *U* respectively being the mean hydraulic radius and mean vertical velocity, is of order $O(10^{-3})$ for all approaches.

It can be noted that EULAG produces higher average vertical velocities (by a factor of about 5/3) with more spatial variability than either SSTOKES or ANSYS FLUENT (Table 1). The mean values associated with SSTOKES and ANSYS FLUENT are essentially the same, and ANSYS FLUENT shows slightly enhanced overall variability with respect to SSTOKES. Values of the Coefficient of Variation (CV) obtained through all three systems are about the same, with ANSYS FLUENT yielding a slightly higher value than the other two.

Linear correlations between horizontal cross-sections of vertical velocity fields produced by the simulation systems are high (> 0.85) at all elevations within the limestone sample (Fig. 3), indicating

a general agreement among the structures of the fields. This is consistent with the values of CV listed in Table 1. Nonetheless, the two-sample Kolmogorov–Smirnov test rejects the hypothesis that the simulated vertical velocities within a cross-section are from the same distribution at the 5% significance level. Correlations between EULAG and the other two systems are somewhat reduced at elevations $(\approx 150-200\,\Delta z)$ where a large decrease in local porosity is observed.

Cross-sectional means and standard deviations of vertical velocities are consistent with the observed pattern resulting in higher velocity and variability for EULAG simulations than for the other two systems (Table 2). The results listed in Table 2 are associated with cross-sections which are all $l \approx 30\,\Delta z$ apart. The mean values associated with ANSYS FLUENT and SSTOKES results coincide and ANSYS FLUENT simulations exhibit somewhat higher standard deviations than SSTOKES does. All three computational systems produce relatively higher (more negative) vertical velocities in the region of low porosity (e.g., at an elevation of about 180 Δz) than at other elevations, and all three show relatively lower (less negative) velocities at elevations (e.g., 215 Δz) where porosity is highest. Similar results (not reported) are obtained on other sets of cross-sections, extracted using the same criteria. Variability, as measured by standard deviation, follows the same pattern of relatively high variability where porosity is lowest (e.g., 180 Δz) and resistance to flow is highest and low variability where porosity is highest and resistance to flow is least.

Contour plots of the vertical velocity component produced by each model in the plane at elevation z = 127 Δz produce similar patterns for the flow field, with EULAG exhibiting higher overall fluxes and more spatial variability in the velocity values than either SSTOKES or ANSYS FLUENT (Fig. 4). In each case the majority of the velocity field is stagnant, or nearly so. This is consistent with the results of [17] who found that most of the flux through a sample of realizations of synthetically generated porous media occurs in a relatively small percentage of the pore volume. Regions of higher velocity in the upper left quadrant and lower middle part, indicated by dark color in Fig. 4, are more finely resolved by ANSYS FLUENT and EULAG than SSTOKES. The sharp gradients that form in the velocity field due to the variable resistance offered by the pore wall geometry are not as apparent

in the solution provided by SSTOKES. Qualitatively similar results are obtained for other planes (not shown).

Scatter plots of values of $|w|$ computed at all nodes within the fluid region by the three methodologies are depicted in Figs. 5a-c. These plots illustrate the general agreement between the ANSYS FLUENT and SSTOKES estimates (values of $|w|$ distributed around the unit slope line) with EULAG estimates that are relatively higher than either (results that consistently lie below this line). Complementary scatter plots of nodal values of fluid pressure are depicted in Figs. 5d-f. These fall on the unit slope line indicating that the three methodologies produce consistently similar results for pressure.

Empirical PDFs of horizontal velocities (u) and normalized vertical velocities ($w/\langle w\rangle$, $\langle\cdot\rangle$ representing sample average) are depicted in Fig. 6a-b. Both PDFs are based on estimates from the whole fluid domain. The horizontal velocity component along the y direction, v, displays similar behavior to u (not shown). Horizontal velocity components from all three simulations display symmetric distributions centered on zero. However, the PDF based on EULAG is characterized by higher tails, indicating a tendency to assign more probability to the tails of the distribution. The normalized vertical velocity component $w/\langle w\rangle$ exhibits clear positive skewness in all three examples, consistent with the gravity-driven flow regime studied. Following [37], a stretched exponential model is juxtaposed to the data in Fig. 6b: the decay of the tails of all three PDFs is consistent with this model, which includes the exponential trend (i.e. linear trend in semi-log scale) as a particular case. The occurrence of only a small fraction of nodes associated with an upward value of w (i.e., negative tail of the PDF) indicates that there is only a limited set of localized recirculation paths in the internal structure of the pore space. When normalized by the sample average, the tail of the PDF obtained using ANSYS FLUENT is slightly higher than that obtained via EULAG or SSTOKES, which is consistent with the CV values listed in Table 1.

377 The three methods yield values for the (macroscopic) mean Darcy flux, q_{ave}, [Eq. (7), averaged
378 over all horizontal cross sections] that are of the same order of magnitude (Table 3). Consistent with
379 the results illustrated in Fig. 5, the estimation of q_{ave} provided by EULAG is larger than those
380 provided by SSTOKES or ANSYS FLUENT.

381 3.2 *Fontainebleau sandstone sample*

382 In general, results of comparisons among simulated states are similar to those observed for the
383 limestone. As in the case of the limestone medium, the three systems produce fluid velocities that are
384 of the same order of magnitude, in this case $O(10^{-5}\ \mathrm{m\,s^{-1}})$, and Reynolds number, which is of order
385 $O(10^{-4})$. EULAG renders higher average vertical velocities (now by a factor of about 2) with more
386 spatial variability than either SSTOKES or ANSYS FLUENT, as shown by the results listed in Table
387 4. The mean values rendered by SSTOKES and ANSYS FLUENT are also essentially coinciding,
388 with SSTOKES showing slightly more pronounced overall variability than ANSYS FLUENT. The
389 CVs produced by all three systems are very similar also in this case, with SSTOKES yielding a
390 slightly higher value than the ANSYS FLUENT or EULAG for this sample. Simulation results of
391 vertical velocity in the sandstone medium are intrinsically more variable than those observed in the
392 more porous limestone.

393 Linear correlations between horizontal cross-sections of vertical velocity fields produced by the
394 simulation systems are high (> 0.85) at all elevations, except over the set of elevations (~120-180 Δz)
395 where porosity increases abruptly (Fig. 7). Correlations between all three pairs of the simulations are
396 considerably reduced there, with the EULAG-SSTOKES pair being least affected. Similar to what is
397 noticed for the limestone rock sample, the two-sample Kolmogorov-Smirnov test rejects the
398 hypothesis that the simulated vertical velocities within any given cross-section are from the same
399 distribution at the 5% significance level.

400 Cross-sectional means and standard deviations of vertical velocities are in line with the general
401 pattern of higher velocity and variability in EULAG simulations (Table 5). The means of ANSYS

FLUENT and SSTOKES estimates are again practically the same, but this time it is the SSTOKES simulations that exhibit somewhat higher standard deviations than ANSYS FLUENT. All three systems produce relatively lower (less negative) vertical velocities in the region of high porosity (e.g., at elevation $z = 140\ \Delta z$) than at other elevations. Similar results (not reported) are obtained on other sets of cross-sections extracted using the same criteria as above. Variability, as measured by standard deviation, follows the same pattern of relatively high variation where porosity is lowest and resistance to flow is highest and low variability where porosity is highest and resistance to flow is least.

Contour plots of simulated vertical velocities in the plane at the middle elevation $z = 127\ \Delta z$ produce roughly similar patterns for the flow field (Fig. 8). The majority of the velocity field is stagnant, or nearly so, with highest flows occurring in the middle of the large pore spanning the cross-section and in the isolated pore toward the bottom, consistent with the observation of [17] that flow in pore spaces tends to occur in a relatively small percentage of the pore volume. EULAG exhibits higher flow overall and more variability than either SSTOKES or ANSYS FLUENT.

Scatter plots of values of $|w|$ computed at all nodes within the fluid region by the three methodologies are depicted in Figs. 9a-c. As in the case of the limestone sample, these illustrate the general agreement between the ANSYS FLUENT and SSTOKES estimates, EULAG estimates being relatively higher than either. Scatter plots of nodal values of fluid pressure are depicted in Fig. 9d-f. These are close to the line of unit slope indicating again that the three methodologies produce consistently similar results for pressure.

Empirical PDFs (Figure 10a-b) of horizontal, u, and normalized vertical, $w/\langle w \rangle$, velocities are based on estimates from the whole fluid domain, which is consistent with the analysis of the limestone sample. The PDF for u is symmetric and centered on zero, and EULAG distributes more probability to the tails of the distribution than either SSTOKES or ANSYS FLUENT. The normalized vertical velocity component is again skewed in the direction of flow. Figure 10b highlights that, similar to what observed for the limestone, the positive tails of the normalized velocity components decay

following a stretched exponential model [37]. In this case the tail of the PDF obtained using ANSYS FLUENT is slightly lower than that associated with the other two samples.

The value of the mean Darcy flux q_{ave} provided by EULAG exceeds those resulting from SSTOKES and ANSYS FLUENT by a factor of about two (see Table 3).

4 Summary and conclusions

Direct numerical simulations of fully-saturated, gravity-driven flow are performed in millimeter-scale digitally reconstructed images of a high-porosity (31%) limestone sample and a low-porosity (7%) sandstone sample using three different Eulerian approaches: (*a*) ANSYS FLUENT (*b*) the EULAG system, and (*c*) the SSTOKES code. These computational systems vary widely in terms of their algorithmic complexity and differ in terms of the associated numerical methodologies, enforcement of no-slip boundary conditions on internal walls, parallelization, and implementation of the Poisson solver. The resulting steady-state flow solutions are compared in terms of global quantities, the empirical probability density function (PDF) and associated main statistical moments of the local velocity fields.

When performing comparisons of computational results obtained with diverse codes the notion of accuracy is poorly defined without a benchmark against which the solutions can be compared. Because nowadays we still do not have at our disposal high quality and high resolution laboratory flow experimental data against which a pointwise comparison of calculated quantities can be accomplished in real rock samples of the size we consider, it is virtually impossible to state without ambiguities if one solution is more accurate than another one. However, the distributions of velocity can be probed to assess similarities and differences between the computational methods. To do so, we consider the local structure of the velocity field, empirical PDFs of vertical and horizontal components of velocity and pressure, the first two moments of the velocity distributions, as well as the cross-correlation coefficient between the vertical velocities rendered by the codes we analyze at level planes. Beyond first order comparisons, such as the mean Darcy flux, the higher order moments

and cross-correlations provide information about the structure and similarities of the velocities fields in a statistical sense.

Given that the methods are notably different in a number of ways, it is remarkable that they produce results that are reasonably close to one another. Using the metrics mentioned above it was observed that the simulation results are similar with respect to (*i*) the overall structure of the empirical PDF of horizontal and vertical velocity components (Figs. 6 and 10), (*ii*) the structure of the spatial distribution of velocities as revealed by cross-correlations (Figs. 3 and 7) and pattern (Figs. 4 and 8), and (*iii*) the magnitude of macroscopic parameters, specifically mean Darcy flux (Table 3), although they differ in details. Notably, the Darcy fluxes computed by the three methodologies are all of the same order of magnitude for a given sample. We note that in principle one could estimate Darcy flux on a rock core of characteristic length of the order of 10^{-3} m. A straightforward calculation shows that in case of such a rock sample the relative measurement errors on permeability and flux would be of about 130% and 250%, respectively. However, these estimates should only be considered as purely theoretical since setting up such measurements is highly difficult with currently available resources, due to (*a*) difficulties in the preparation of the sample and (*b*) the smallness of the pressure drop, which is notably complex to be measured. On the basis of these considerations, we conclude that Darcy flux values obtained using the computational suites considered would be within theoretical bounds associated with what would be a hypothetical laboratory experiment on millimeter-scale samples.

The three simulation environments produce steady-state flow fields that differ in their local details. When considering the pore-scale quantities associated with the Mondeville limestone, the similarity between the solutions obtained using ANSYS FLUENT and EULAG suggests that steep gradients in the velocity field, which result from the wider pores and non-uniform resistance offered by the variable geometry of the pore space, are more finely resolved when the nonlinear term in the Navier-Stokes equations is retained (Figs. 3 and 4). In the case of the Fontainebleau sandstone, the structure of the velocity fields obtained using EULAG and SSTOKES agree more than either does

478 with ANSYS FLUENT (Figs. 7 and 8). In this low porosity sample, solutions obtained using EULAG
479 and SSTOKES capture the spatial influence of the geometry and topology of the pore space on the
480 velocity field.

481 When considering up-scaling of flow solutions to macroscopic quantities, including Darcy flux
482 and thus permeability, the most relevant difference among the methodologies is the relatively large
483 flow velocities computed by EULAG compared to ANSYS FLUENT and SSTOKES (Figs. 5 and 9
484 and Table 3). We also note that if simulation of pore-scale flow is aimed at understanding the
485 influence of pore space geometry and topology on local fluid dynamics, then EULAG appears to
486 provide consistent results with respect to structure and variability of the velocity fields in these two
487 samples. The computed Reynolds numbers, $O(10^{-3}/10^{-4})$, might not be completely consistent with the
488 assumptions upon which the Stokes equation rests. The observed difference in Darcy flux between
489 EULAG and FLUENT could also result from the adopted numerical scheme to resolve the advective
490 term in the corresponding momentum equations. FLUENT uses an upwinding scheme, which are
491 numerically diffusive, and could result in the underestimation of the flux due to numerical diffusion.
492 Otherwise, EULAG uses a nonlinear flux-limiting advection scheme to resolve high gradients and
493 minimize numerical diffusion, which is consistent with the highest value obtained for the Darcy flux.
494 This notwithstanding, we remark that the computed values could still be considered as comprised
495 within theoretical laboratory measurement error bounds, as discussed above.

496 When compared across the two media investigated here, the Darcy fluxes in the limestone (see
497 Table 3) sample are larger than those computed for the sandstone, consistent with the significant
498 difference between the porosities (31% to 7%) of the two rock samples. The associated empirical
499 PDFs of horizontal components, u, and normalized vertical components, $w/\langle w \rangle$, of velocity are
500 qualitatively similar (Figs. 6 and 10). The positive skewness of the PDFs of $w/\langle w \rangle$ obtained from all
501 three simulations (Figs. 6b and 10b) reflects the dominant downward direction (i.e., in the direction
502 of the negative z-axis) of flow, consistent with the gravity-driven flow regime studied. In general the
503 three computational systems analyzed produce normalized vertical velocities exhibiting about the

same level of variability. This similarity indicates that the intrinsic variability of the results among these computational systems arises primarily from a multiplicative effect that is cancelled through normalization by the means. The small fraction of nodes associated with a positive value of *w* (the negative tail of the PDF) suggests that there is only a limited set of localized recirculation paths in the pore spaces of both media. The tails corresponding to simulated values of *u* produced by EULAG are larger in both media than the tails associated with ANSYS FLUENT or SSTOKES (Figs. 6a and 10a). This is consistent with observations of generally higher degree of heterogeneity of the state of flow arising from the EULAG-based simulations.

As a general conclusion, these comparisons indicate that the three computational systems produce consistent estimates of the state of flow through explicit natural porous microstructures. This is observed despite the considerable differences among the three solution techniques. The correspondence among the results supports the reliability of employing computational approaches to perform detailed simulations of flow dynamics in complex pore spaces of the kind associated with high definition imaged rock systems which are becoming increasingly available due to the advancement of digital rock physics techniques.

References

1. Angot, P., Bruneau, C.H., Fabrie, P.: A penalization method to take into account obstacles in incompressible viscous flows. Numer. Math. **81**, 497-520 (1999)
2. ANSYS, Inc.: ANSYS® FLUENT® User's guide, Rel. 12.1 (2009)
3. Barth, T., Jespersen, D.: The design and application of upwind schemes on unstructured meshes. AIAA Paper **89-0366**, 27th Aerospace Sciences Meeting, Reno, NV, USA (1989)
4. Blunt, M.J., Bijeljic, B., Dong, H., Gharbi, O., Iglauer, S., Mostaghimi, P., Paluszny, A., Pentland, C.: Pore-scale imaging and modeling. Adv. Water Resour. **51**, 197-216 (2013)
5. Blunt, M.J., Jackson, M.D., Piri, M., Valvatne, P.H.: Detailed physics, predictive capabilities and macroscopic consequences for pore-network models of multiphase flow. Adv. Water Resour. **25**, 1069-1089 (2002)

530 6. Boek, E.S., Venturoli, M.: Lattice-Boltzmann studies of fluid flow in porous media with
531 realistic rock geometries. Comput. Math. Appl. **59**, 2305-2314 (2010)
532 7. Bourbié, T., Zinszner, B.: Hydraulic and acoustic properties as a function of porosity in
533 Fontainebleau sandstone. J. Geophys. Res. **90**, 11524-11532 (1985)
534 8. Chen, S., Doolen, G.D.: Lattice Boltzmann method for fluid flows. Annu. Rev. Fluid Mech.
535 **30**(1), 329–364 (1998)
536 9. Coon, E.T., Porter, M.L., Kang, Q.: Taxila LBM: a parallel, modular lattice Boltzmann
537 framework for simulating pore-scale flow in porous media. Comput. Geosci. **18**, 17–27 (2014)
538 10. Fourie, W., Said, R., Young, P., Barnes, D.L.: The Simulation of Pore Scale Fluid Flow with
539 Real World Geometries Obtained from X-Ray Computed Tomography. In: Proceedings of the
540 COMSOL Conference (2007)
541 11. Gerbaux, O., Buyens, F., Mourzenko, V.V., Memponteil, A., Vabre, A., Thovert, J.F., Adler,
542 P.M.: Transport properties of real metallic foams. J. Colloid Interf. Sci. **342**, 155-165 (2010)
543 12. Goldstein, D., Handler, R., Sirovich, L.: Modeling a no-slip flow boundary with an external
544 force field. J. Comput. Phys. **105**, 354-366 (1993)
545 13. Gouze, P., Luquot, L.: X-ray microtomography characterization of porosity, permeability and
546 reactive surface changes during dissolution. J. Contam. Hydrol. **120-121**, 45-55 (2010)
547 14. Gouze, P., Melean, Y., Le Borgne, T., Dentz, M., Carrera, J.: Non-Fickian dispersion in porous
548 media explained by heterogeneous microscale matrix diffusion. Water Resour. Res. **44**,
549 W11416 (2008)
550 15. Griebel, M., Klitz, M.: Homogenization and numerical simulation of flow in geometries with
551 textile microstructures. Multiscale Model Sim. **8**(4), 1439–1460 (2010)
552 16. Guo, Z., Zhao, T.S., Shi, Y.: Preconditioned lattice-Boltzmann method for steady flows. Phys.
553 Rev. E **70**, 066706 (2004)
554 17. Hyman, J.D., Smolarkiewicz, P.K., Winter C.L.: Heterogeneities of flow in stochastically
555 generated porous media. Phys. Rev. E **86**, 056701 (2012)

556 18. Hyman, J.D., Smolarkiewicz, P.K., Winter C.L.: Pedotransfer functions for permeability: a
557 computational study at pore scales. Water Resour. Res. **49**, 2080-2092 (2013)
558 19. Hyman, J.D., Winter C.L.: Hyperbolic regions in flows through three-dimensional pore
559 structures. Phys. Rev. E **88**, 063014 (2013)
560 20. Hyman, J.D., Winter C.L.: Stochastic generation of explicit pore structures by thresholding
561 Gaussian random fields. J. Comput. Phys. **277**, 16-31 (2014)
562 21. Icardi, M., Boccardo, G., Marchisio, D.L., Tosco, T., Sethi, R.: Pore-scale simulation of fluid
563 flow and solute dispersion in three-dimensional porous media. Phys. Rev. E **90**, 013032 (2014)
564 22. Issa, R.I.: Solution of the implicitly discretized fluid flow equations by operator-splitting. J.
565 Comput. Phys. **62**, 40-65 (1986)
566 23. Kang, Q., Lichtner P.C., Zhang D.: Lattice Boltzmann pore-scale model for multicomponent
567 reactive transport in porous media. J. Geophys. Res. **111**, B05203 (2006)
568 24. Lopez Penha, D.J., Geurts, B.J., Stolz, S., Nordlund, M.: Computing the apparent permeability
569 of an array of staggered square rods using volume-penalization. Comput. Fluids **51**, 157-173
570 (2011)
571 25. Malico, I., Ferreira de Sousa, P.J.S.A.: Modeling the pore level fluid flow in porous media using
572 the Immersed Boundary method. In: Delgado, J.M.P.Q. et al. (eds). Numerical Analysis of Heat
573 and Mass Transfer in Porous Media, Advanced Structured Materials 27, pp. 229-251. Springer,
574 Heidelberg (2012)
575 26. Manwart, C., Aaltosalmi, U., Koponen, A., Hilfer, R., Timonen, J.: Lattice-Boltzmann and
576 finite-difference simulations for the permeability for three-dimensional porous media. Phys.
577 Rev. E **66**, 016702 (2002)
578 27. Mittal, R., Iaccarino, G.: Immersed-boundary methods. Ann. Rev. Fluid Mech. **37**, 239-261
579 (2005)
580 28. Mostaghimi, P., Blunt, M.J., Bijeljic, B.: Computations of absolute permeability on micro-CT
581 images. Math. Geosci. **45**, 103–125 (2013)

582 29. Ovaysi, S., Piri, M.: Direct pore-level modeling of incompressible fluid flow in porous media.
583 J. Comput. Phys. **229**(19), 7456 – 7476 (2010)
584 30. Pan, C., Hilpert, M., Miller, C.T.: Lattice-Boltzmann simulation of two-phase flow in porous
585 media. Water Resour. Res. **40**, W01501 (2004)
586 31. Pan, D., Shen, T.T.: Computation of incompressible flows with immersed bodies by a simple
587 Ghost Cell method. Int. J. Numer. Meth. Fluids **60**, 1378–1401 (2009)
588 32. Peszynska, M., Trykozko, A.: Pore-to-core simulations of flow with large velocities using
589 continuum models and imaging data. Comput. Geosci. **17**, 623–645 (2013)
590 33. Prusa, J.M., Smolarkiewicz, P.K., Wyszogrodzki, A.A.: EULAG, a computational model for
591 multiscale flows. Comput. Fluids. **37**, 1193-1207 (2008)
592 34. Raoof, A., Hassanizadeh, S.M.: A new formulation for pore-network modeling of two-phase
593 flow. Water Resour. Res. **48**, W01514 (2012)
594 35. Sarkar, S., Toksöz, M.N., Burns, D.R.: Fluid Flow Simulation in Fractured Reservoirs. Report,
595 Annual Consortium Meeting. MIT Earth Resources Laboratory (2002)
596 36. Siena, M., Guadagnini, A., Riva, M., Gouze, P., Smolarkiewicz, P.K., Winter, C.L., Hyman,
597 J.D., Inzoli, F., Guédon, G.R., Colombo E.: A comparison of body-fitted and immersed
598 boundary methods for pore-scale modeling of fully saturated flow in synthetic porous media.
599 In: Proceedings of the IAHR International Groundwater Symposium - Modeling and
600 Management under Uncertainty. Hadi, K., Copty, N.K. (eds.) Taylor and Francis Group,
601 London (2013)
602 37. Siena, M., Riva, M., Hyman, J.D., Winter, C.L., Guadagnini, A.: Relationship between pore
603 size and velocity probability distributions in stochastically generated porous media. Phys. Rev.
604 E **89**, 003000 (2014)
605 38. Smolarkiewicz, P.K.: Multidimensional positive definite advection transport algorithm: An
606 overview. Int. J. Numer. Meth. Fluids **50**, 1123–1144 (2006)

607 39. Smolarkiewicz, P.K., Margolin, L.G.: MPDATA: A finite-difference solver for geophysical
608 flows. J. Comput. Phys. **140**(2), 459–480 (1998)
609 40. Smolarkiewicz, P.K., Prusa, J.M.: Forward-in-time differencing for fluids: simulation of geo-
610 physical turbulence. In: Drikakis, D., Geurts, B.J. (eds.) Turbulent Flow Computation, pp. 279–
611 312. Kluwer Academic Publishers, Netherlands (2002)
612 41. Smolarkiewicz, P.K., Sharman, R., Weil, J., Perry, S.G., Heist, D., Bowker, G.: Building
613 resolving large-eddy simulations and comparison with wind tunnel experiments. J. Comput.
614 Phys. **227**, 633-653 (2007)
615 42. Smolarkiewicz, P.K., Szmelter J.: Iterated upwind schemes for gas dynamics. J. Comput. Phys.
616 **228**(1), 33–54 (2009)
617 43. Smolarkiewicz, P.K., Winter, C.L.: Pore resolving simulation of Darcy flows. J. Comput. Phys.
618 **229**, 3121-3133 (2010)
619 44. Tartakovsky, A.M., Meakin, P.: A smoothed particle hydrodynamics model for miscible flow
620 in three-dimensional fractures and the two-dimensional Rayleigh–Taylor instability. J. Comput.
621 Phys. **207**(2), 610–624 (2005)
622 45. Tartakovsky, A.M., Meakin, P., Scheibe, T.D., Eichler West, R.M.: Simulations of reactive
623 transport and precipitation with smoothed particle hydrodynamics. J. Comput. Phys. **222**(2),
624 654– 672 (2007)
625 46. Tseng, Y.H., Ferziger, J.H.: A ghost-cell immersed boundary method for flow in complex
626 geometry. J. Comput. Phys. **192**, 593-623 (2003)
627 47. Valvatne, P.H., Blunt, M.J.: Predictive pore-scale modeling of two-phase flow in mixed wet
628 media. Water Resour. Res. **40**, W07406 (2004)
629 48. Wildenschild, D., Vaz, C.M.P., Rivers, M.L., Rikard, D., Christensen, B.S.B.: Using X-ray
630 computed tomography in hydrology: systems, resolutions and limitations. J. Hydrol. **267**, 285-
631 297 (2002)

49. Zaretskiy, Y., Geiger, S., Sorbie, K., Förster, M.: Efficient flow and transport simulations in reconstructed 3D pore geometries. Adv. Water Resour. **33**, 1508-1516 (2010)

636

637 **TABLES**

638 **Table 1** Mean, Standard Deviation (SD), and Coefficient of Variation (CV) of vertical velocity
639 summed over all points in the pore space of the Mondeville limestone sample.

	Mean ($\times 10^{-4}$ m s^{-1})	SD ($\times 10^{-4}$ m s^{-1})	CV
EULAG	–3.23	4.55	1.41
SSTOKES	–1.93	2.76	1.43
ANSYS FLUENT	–1.93	3.00	1.55

640

641 **Table 2** Mean and Standard Deviation (SD) computed for four selected cross sections of the
642 Mondeville limestone sample.

	Mean ($\times 10^{-4}$ m s^{-1})			SD ($\times 10^{-4}$ m s^{-1})		
LEVEL	EULAG	SSTOKES	ANSYS FLUENT	EULAG	SSTOKES	ANSYS FLUENT
65	–3.35	–2.02	–2.02	3.56	2.26	2.42
120	–3.81	–2.30	–2.30	5.83	3.79	4.02
180	–6.88	–4.01	–3.99	7.95	4.48	5.05
215	–2.00	–1.20	–1.22	2.59	1.56	1.81

643

644

645 **Table 3** Comparison of mean Darcy flux computed using the three methodologies analyzed.

	Mondeville Limestone	Fontainebleau Sandstone
Model	q_{ave} ($\times 10^{-5}$ m s^{-1})	q_{ave} (10^{-6} m s^{-1})
EULAG	–9.97	-2.16
SSTOKES	–6.06	-1.04
ANSYS FLUENT	–6.08	-1.13

646

647

648

649 **Table 4** Mean, Standard Deviation (SD), and Coefficient of Variation (CV) of vertical velocity
650 summed over all points in the pore space of the Fontainebleau sandstone sample.

	Mean ($\times 10^{-5}$ m s^{-1})	SD ($\times 10^{-5}$ m s^{-1})	CV
EULAG	–3.07	7.90	2.57
SSTOKES	–1.48	4.45	3.01
ANSYS FLUENT	–1.60	3.81	2.38

651

652

653

654 **Table 5** Mean and Standard Deviation (SD) of vertical velocity computed on four selected cross
655 sections of the Fontainebleau sandstone sample.

	Mean ($\times 10^{-5}$ m s^{-1})			SD ($\times 10^{-5}$ m s^{-1})		
LEVEL	EULAG	SSTOKES	ANSYS FLUENT	EULAG	SSTOKES	ANSYS FLUENT
50	–0.57	–0.28	–0.25	0.46	0.27	0.19
100	–0.46	–0.23	–0.24	1.44	0.81	0.71
140	–0.11	–0.05	–0.07	0.19	0.11	0.11
200	–0.52	–0.26	–0.26	1.68	0.99	0.84

656

657

658

FIGURES

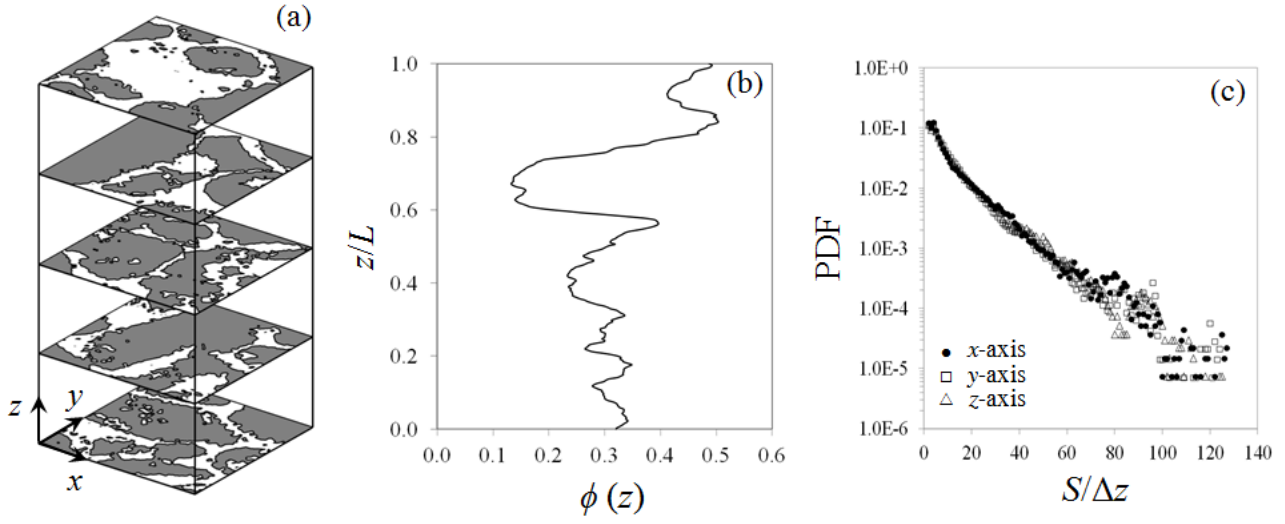

Fig. 1 Mondeville limestone: (a) Horizontal cross sections, white regions represent the pore space; (b) Vertical distribution of surface porosity; (c) empirical Probability Density Functions (PDFs) of pore sizes, S, normalized by the grid step, $\Delta z = 5.06$ µm, evaluated along the three Cartesian axes, x, y and z, and computed on the whole domain.

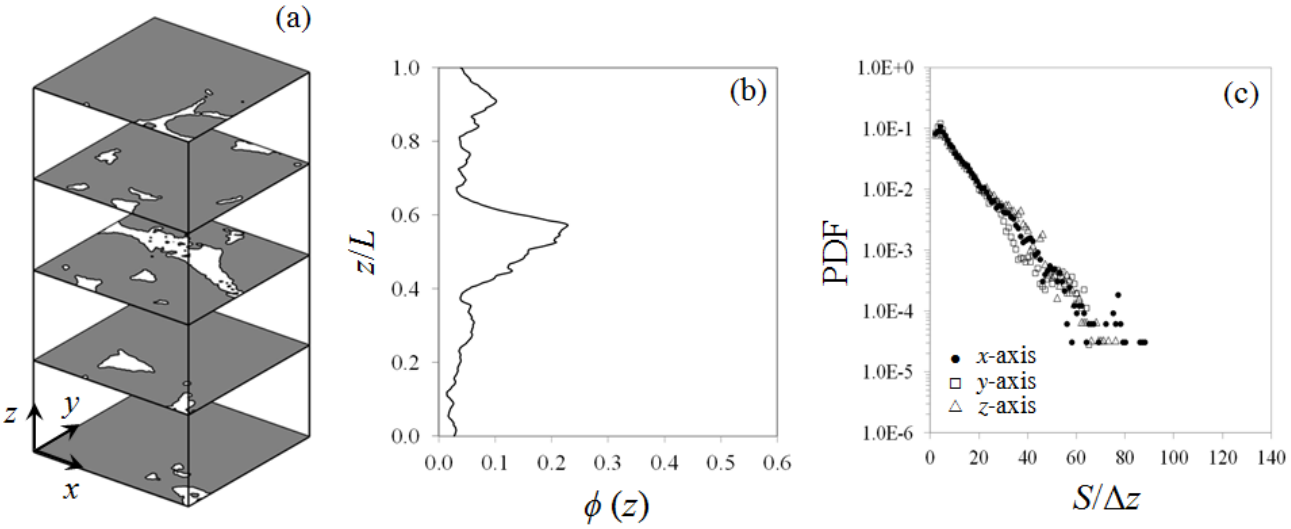

Fig. 2 Fontainebleau sandstone: (a) Horizontal cross sections, white regions represent the pore space; (b) Vertical distribution of surface porosity; (c) empirical Probability Density Functions (PDFs) of pore sizes, S, normalized by the grid step, $\Delta z = 5.06$ µm, evaluated along the three Cartesian axes, x, y and z, and computed on the whole domain.

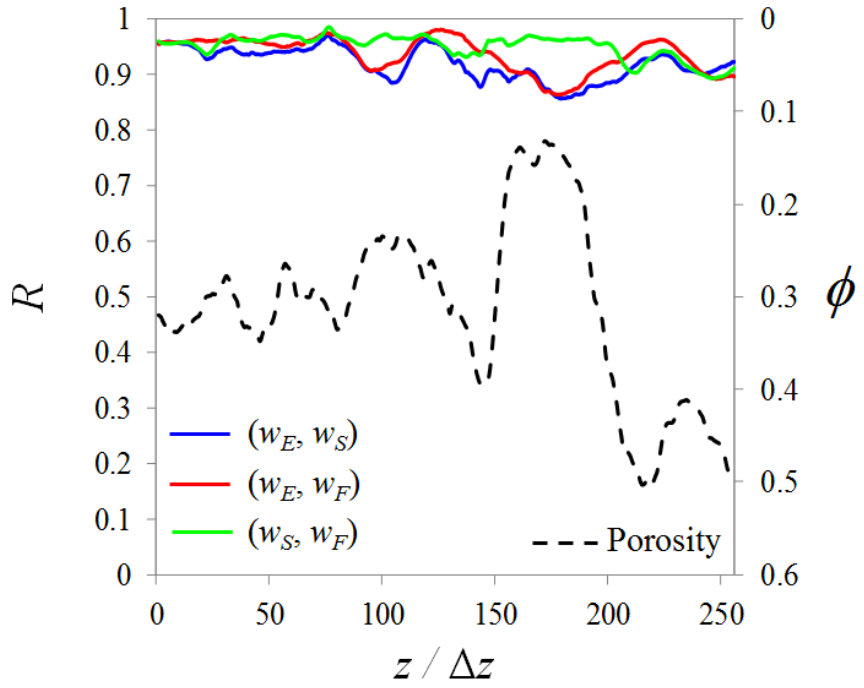

Fig. 3 Mondeville limestone. Cross-correlation coefficients R by vertical level of the cross-section (here w_E, w_S, and w_F respectively denote vertical velocities computed by means of EULAG, SSTOKES or ANSYS FLUENT). The vertical profile of porosity, ϕ, is also reported.

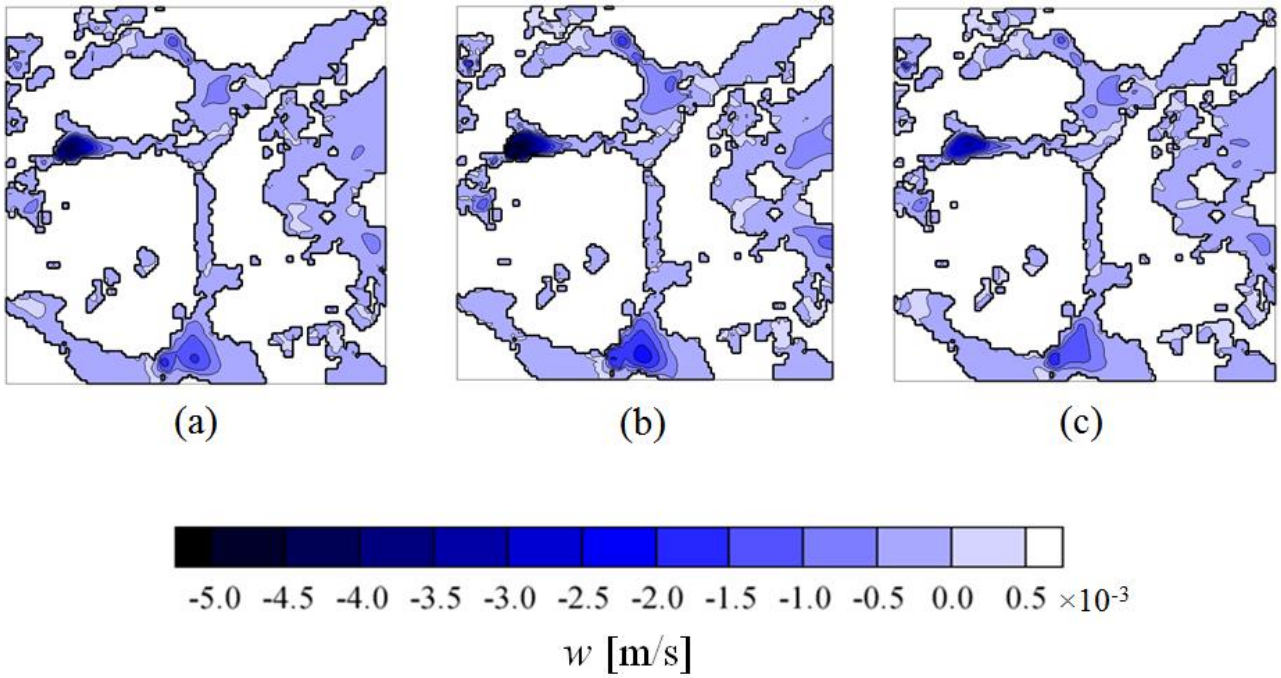

Fig. 4 Spatial distribution of the vertical velocity component, w, obtained by (a) ANSYS FLUENT, (b) EULAG, and (c) SSTOKES along the plane at elevation $z = 127\Delta z$ of Mondeville limestone.

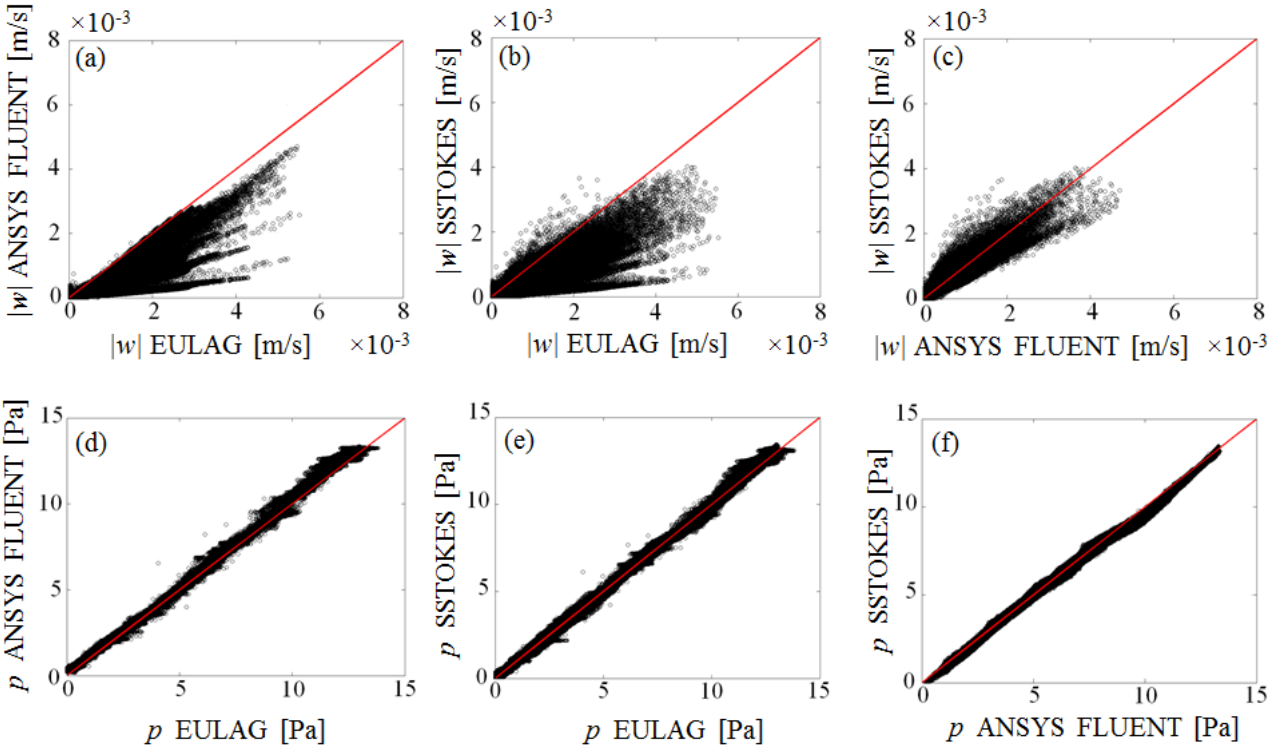

677

678 **Fig. 5** Scatter diagrams of values of (a-c) $|w|$ and (d-f) p computed at the nodes within the fluid region

679 by the three methodologies analyzed for Mondeville limestone.

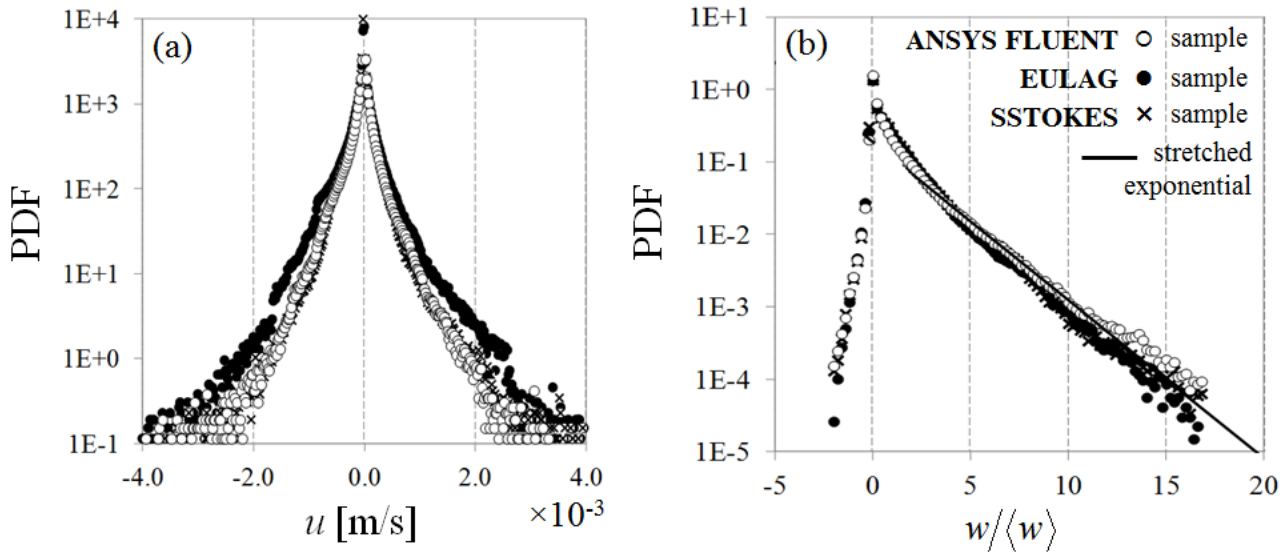

680

681 **Fig. 6** Empirical PDF of (a) u and (b) $w/\langle w \rangle$ - where $\langle \cdot \rangle$ represents sample average - computed over

682 the whole fluid domain with the three methodologies analyzed for Mondeville limestone.

683

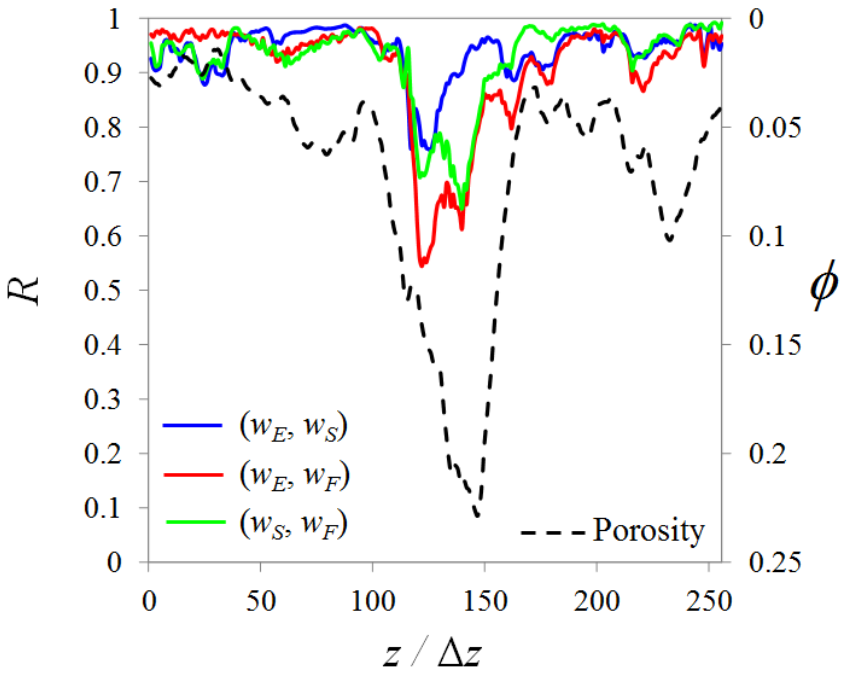

684

685 **Fig. 7** Fontainebleau sandstone. Cross-correlation coefficients R by vertical level of the cross section

686 (here w_E, w_S, and w_F respectively denote vertical velocities computed by means of EULAG,

687 SSTOKES or ANSYS FLUENT). The vertical profile of porosity, ϕ, is also reported.

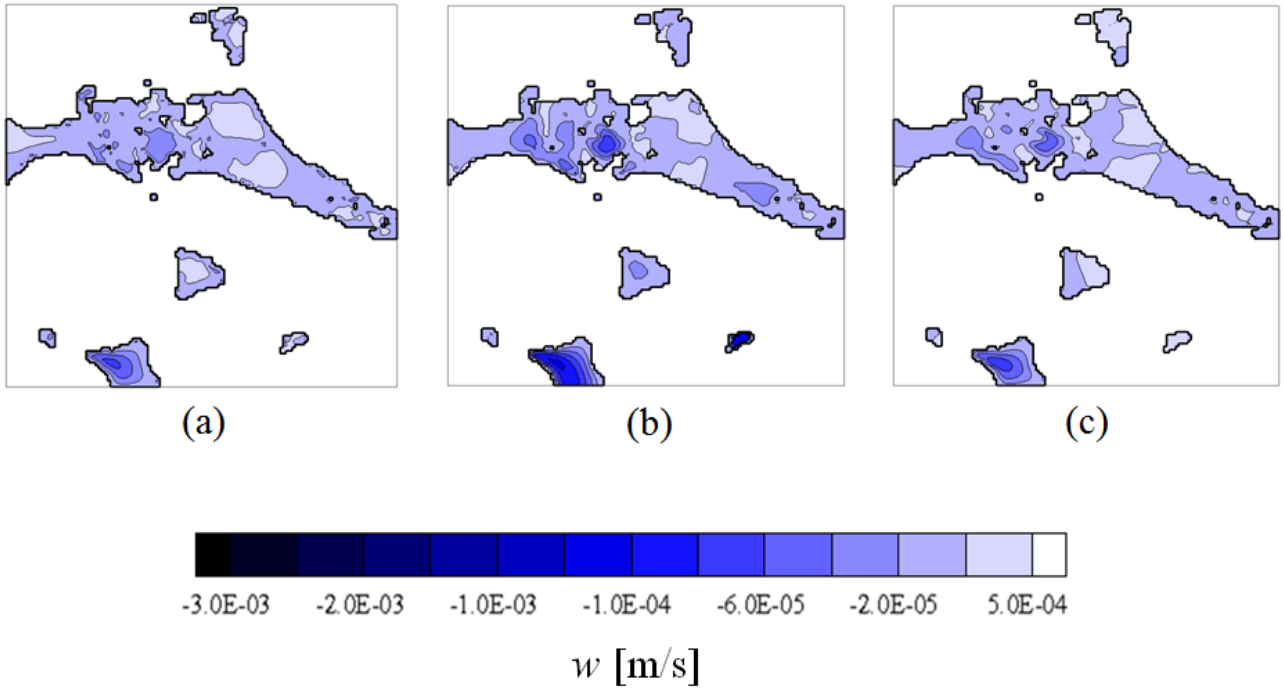

688

689 **Fig. 8** Spatial distribution of the vertical velocity component, w, obtained by (a) ANSYS FLUENT,

690 (b) EULAG, and (c) SSTOKES along the plane at elevation $z = 127\Delta z$ of Fontainebleau sandstone.

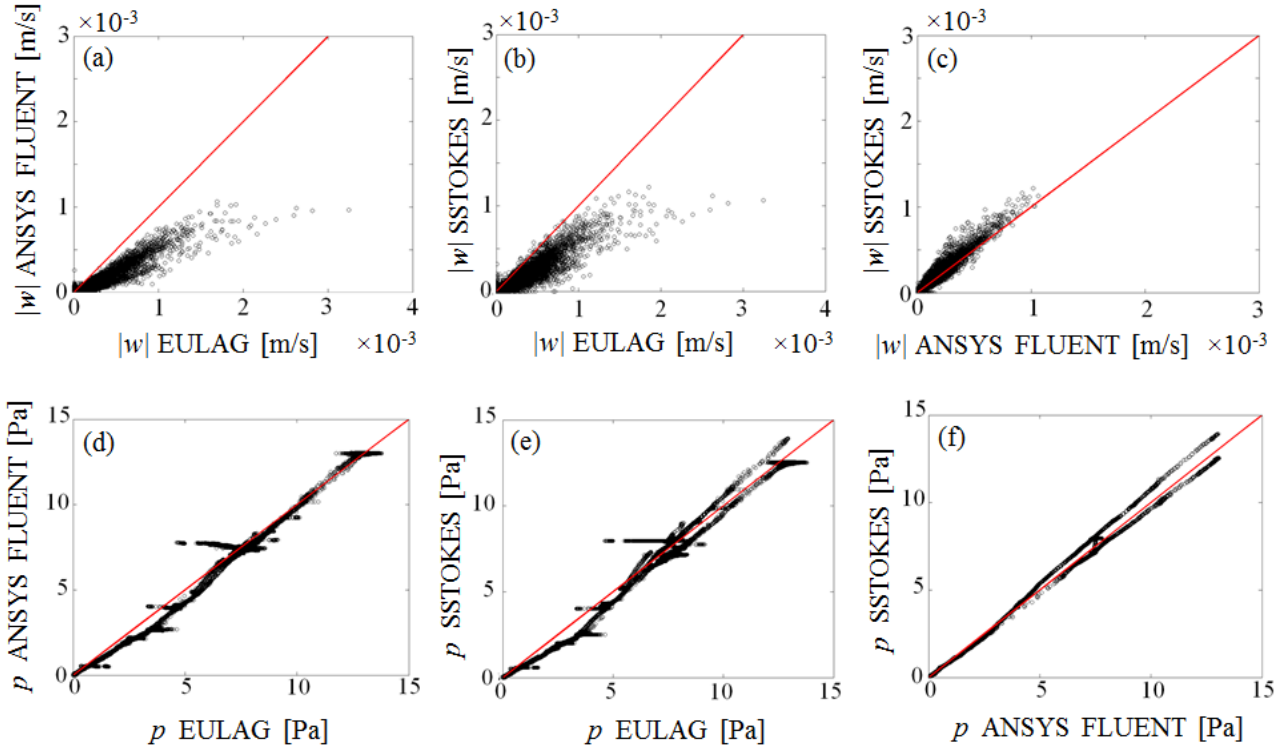

691

692 **Fig. 9** Scatter diagrams of values of (a-c) $|w|$ and (d-f) p, computed at the nodes within the fluid

693 region by the three methodologies analyzed for Fontainebleau sandstone.

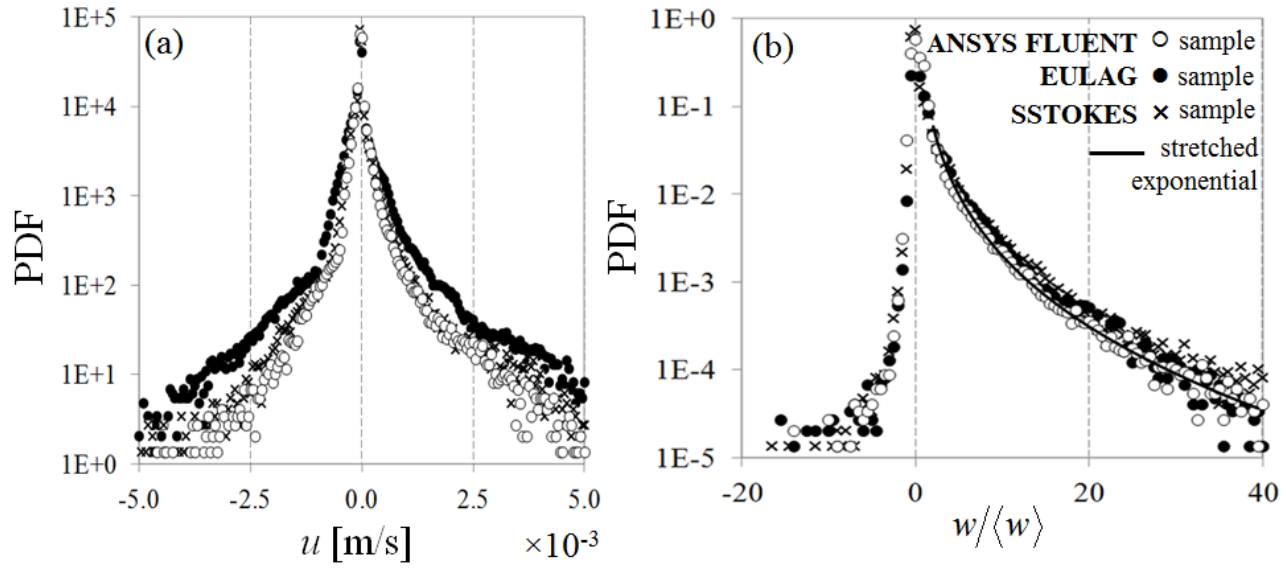

694

695 **Fig. 10** Empirical PDF of (a) u and (b) $w/\langle w \rangle$ - where $\langle \cdot \rangle$ represents sample average - computed over

696 the whole fluid domain with the three methodologies analyzed for Fontainebleau sandstone.

697